ACS NANO

www.acsnano.org

ARTICLE

Ultralow Shrinkage 3D Transparent Nanoporous Glass Printing through Low-Temperature Sintering for Micro-Optical Applications

Yuan Tao, Xinyi Gu, Hao Wu, Jincheng Ni, Yanlei Hu, Dong Wu, Jiaru Chu, and Jiawen Li*

Cite This: *ACS Nano* 2025, 19, 31643–31655

Read Online

ACCESS | Metrics & More | Article Recommendations | Supporting Information

ABSTRACT: **Current glass additive manufacturing relies on high-temperature processing to achieve optical transparency accompanied by significant structural shrinkage. These factors significantly restrict the micro-optical applications of three-dimensional (3D) glass microstructures in microsystems. Here, a low-temperature, low-shrinkage 3D printing strategy for transparent nanoporous glass microstructures is presented using a molecular cross-linker-free resin containing methacrylic acid-functionalized nanoparticles (MAA-NPs). The MAA-NPs serve dual roles as photopolymerizable units and silica precursors, enabling the creation of 3D microarchitectures with a 78 wt % solid loading through two-photon polymerization. In stark contrast to conventional particle-loaded composites, uniform nanoparticle dispersion eliminates wavelength-scale pores in the microstructure after sintering at 650 °C, achieving 97% visible-light transmittance. Most importantly, the combination of MAA cross-linking, which enables small interparticle spacing, and low-temperature sintering results in nanoporous glass 3D microarchitectures with low linear shrinkage (~5%), thereby enabling high-fidelity fabrication of complex micro-optics. Crucially, our strategy enables direct in situ integration of glass microlenses on optical fibers at low temperatures, achieving high alignment precision without assembly steps. This strategy exhibits potential across multiple domains, including micro-optics, photonics, biomedical devices, and integrated optics.**

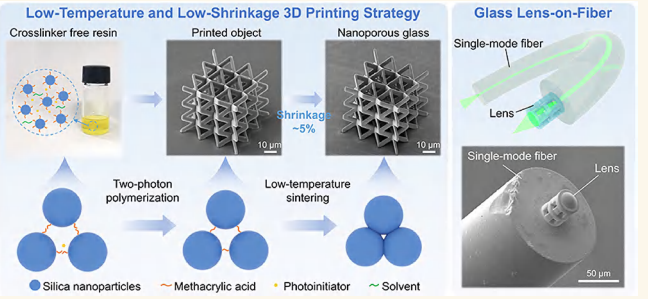

KEYWORDS: *two-photon polymerization, 3D transparent glass microstructure, low shrinkage, low-temperature sintering, optical fiber integrated microdevices*

Glasses, such as fused silica glass, nanoporous glass, and multicomponent glass, possess exceptional properties, including outstanding optical transparency and environmental robustness, making them indispensable in contemporary scientific and industrial fields.[1−3] Shaping these glasses into desired geometries, especially three-dimensional (3D) structures with precisely defined micro/nanoscale features, can significantly propel the development of advanced applications, such as micro-optics,[4,5] photonics,[6] microelectromechanical systems,[7] and microfluidics.[8,9] Notably, 3D glass microstructures hold great promise in micro-optical applications, as they can replace original polymer components to achieve enhanced stability and performance. Especially, the integration of glass micro-optics into microsystems can extend their service lifetime and broaden their application scope to harsh operational environments.[10−14] Current state-of-the-art glass manufacturing methodologies rely on additive manufacturing to fabricate silica-based hybrid structures, which are subsequently converted into transparent glass through thermal processing.[15−27] However, the reliance on high-temperature treatments (>1100 °C) imposes significant constraints on the direct integration of glass microcomponents into microsystems, as most substrates cannot withstand such high temperatures. Thus, current glass additive manufacturing methods have limited integration compatibility, which hinders the expansion of application fields.

Received: June 4, 2025
Revised: August 15, 2025
Accepted: August 18, 2025
Published: August 22, 2025

https://doi.org/10.1021/acsnano.5c09272
ACS Nano 2025, 19, 31643−31655

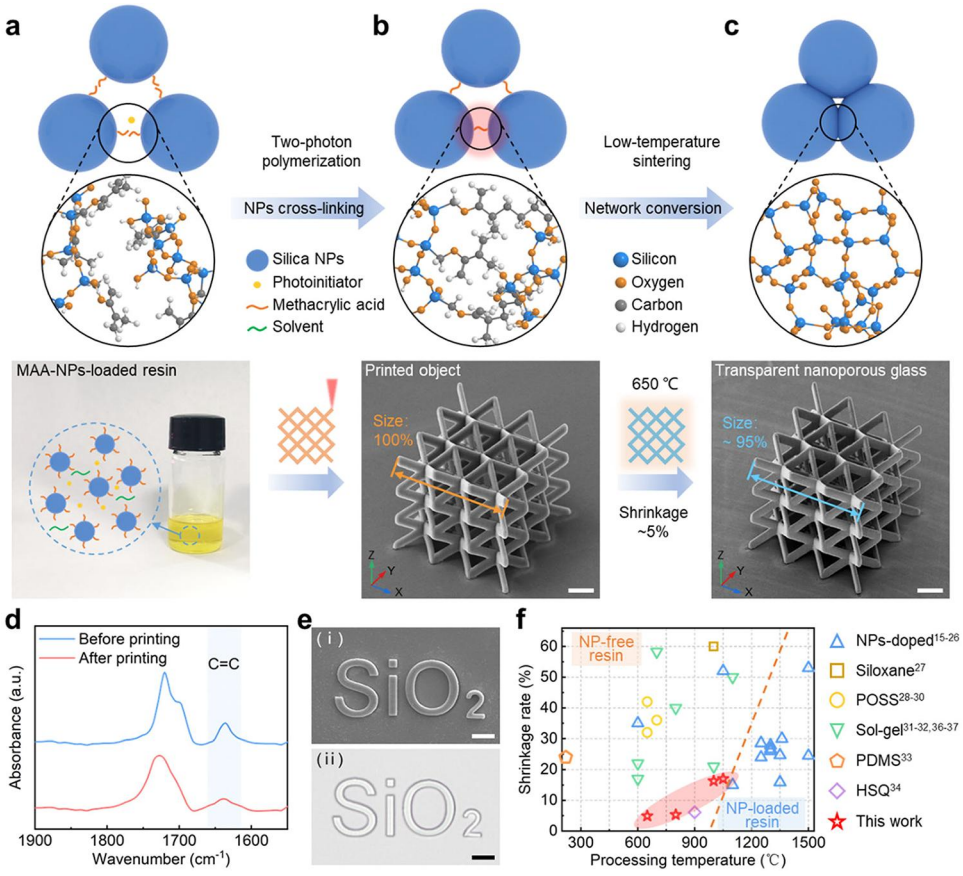

Figure 1. Low-temperature and low-shrinkage fabrication of transparent nanoporous silica glass microstructures. (a–c) Schematic illustration of the state evolution of NPs during TPP and low-temperature sintering. Scale bars: 10 μm. (d) FTIR spectra of the samples before and after printing in the range of 1550–1900 cm^{-1}. The C=C elongation at 1636 cm^{-1} exhibits a decrease as expected from polymerization. (e) SEM and optical microscopy images of the nanoporous glass micropattern "SiO_2", demonstrating no deformation and excellent optical transparency. Scale bars, 10 μm. (f) Plot of the shrinkage rate against the processing temperature of the 3D-printed transparent glass in our work, together with the data of other reported 3D-printed transparent glasses for comparison.[15−34,36,37]

Low-temperature or nonthermal processing methods can significantly popularize the application of glass 3D printing in microsystems. To this end, particle-free silica-based resins, such as polyhedral oligomeric silsesquioxane (POSS)[28−30] and sol−gel materials,[31,32] polydimethylsiloxane (PDMS),[33] and hydrogen silsesquioxane (HSQ),[34,35] have been proposed to reduce the high temperatures required for particle sintering. Despite the promising potential of these materials, critical temperature limitations persist in the most widely used particle-loaded nanocomposites, which typically reveal poor transparency and mechanical strength after thermal treatments below 700 °C.[20−22] It inhibits more cost-effective and widely used material systems from achieving technological breakthroughs in advanced glass applications. Moreover, due to the high organic content, existing silica-based materials generally have low loading capacities (<60 wt %), which exacerbates structural shrinkage (>20%).[16,23,28,36,37] Such significant shrinkage compromises the shape fidelity and positional accuracy of 3D printed microstructures, leading to nonuniform mechanical or optical properties.[38−40] The combination of appropriate processing temperatures and deformation-free geometries is expected to further expand the application fields of transparent glass. Therefore, it is highly desirable and challenging to develop a strategy that can simultaneously achieve high transparency and low shrinkage in 3D printed glass structures through low-temperature processing.

Achieving this goal requires a resin system with a high packing density of small-sized nanoparticles (NPs), where the small nanoparticle size facilitates low-temperature sintering[41,42] and the high particle loading minimizes shrinkage. Recently, monomer-functionalized NPs with photoresponsive properties have garnered significant attention. These functional groups enable copolymerization with acrylic-based polymers to enhance mechanical performance, demonstrating promising applications in dental materials[43] and 3D printing.[44] Crucially, in the absence of polymers, monomer-functionalized NPs can serve as individual photopolymerizable units for photopolymerization-based printing,[45,46] yielding polymerized architectures with high nanoparticle packing density. Therefore, this material system offers a viable pathway toward maximizing nanoparticle loading capacity while enabling low-temperature, minimal-shrinkage fabrication of transparent glass. Here, we present a strategy for low-temperature, low-shrinkage 3D printing of transparent nanoporous glass microstructures using a resin doped with methacrylic acid-functionalized silica nanoparticles (MAA-NPs) to address the above challenge. Our resin is a molecular cross-linker-free resin, which can achieve photopolymerization through methacrylic acid (MAA) functional groups on the surface of NPs, reaching a solid content of 78 wt %. Owing to this unique feature, microstructures fabricated through two-photon polymerization (TPP) exhibit uniform and densely packed nanoparticle

https://doi.org/10.1021/acsnano.5c09272
ACS Nano 2025, 19, 31643−31655

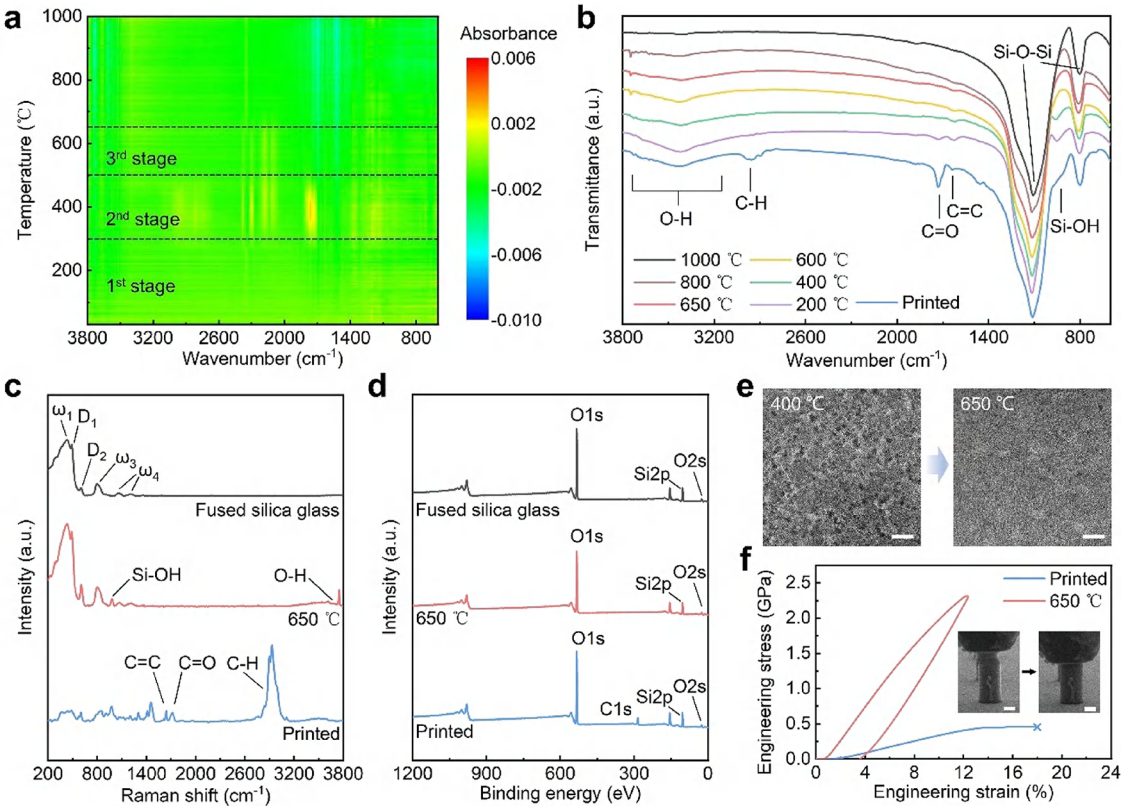

Figure 2. Chemical and physical characterizations of low-temperature sintered nanoporous silica glass. (a) FTIR spectra of the gases released from the printed samples as the temperature increased from room temperature to 1000 °C. Almost all organic compounds decomposed at 650 °C. (b) FTIR spectra of the printed samples after heat treatment at different temperatures. (c) Comparison of Raman spectra of printed, 650 °C sintered, and commercial fused silica glass. The Raman spectrum of the 650 °C sintered sample is similar to that of the commercial reference, indicating successful conversion to a silica network. (d) Comparison of XPS spectra of printed, 650 °C sintered, and commercial fused silica glass. The carbon peak is completely removed in the 650 °C sintered sample, confirming the elimination of organic residues. (e) Bright-field TEM images of the 400 and 650 °C sintered glass, confirming a uniformly distributed nanoporous internal characteristic. Scale bars, 20 nm. (f) Measured compressive stress−strain curves of printed and 650 °C sintered micropillars. The 650 °C sintered micropillar exhibits enhanced mechanical strength compared to the printed sample. Scale bars: 2 μm.

arrangements. This ultimately enables the 650 °C sintered structures to demonstrate 97% visible-light transmittance with a linear shrinkage as low as 5%. The strategy achieves the successful fabrication of high-fidelity complex 3D micro-architectures and functional micro-optics. Furthermore, glass microlenses are integrated on the end of optical fibers in situ without assembly steps, demonstrating the application potential of our strategy in microsystems. Overall, our strategy paves an alternative route for low-temperature 3D glass manufacturing and unveils significant application prospects in integrated optics microdevices.

RESULTS AND DISCUSSION

Resin Formulation and Printing Mechanism. As illustrated in Figure 1a, our resin solely consists of MAA-NPs, a photoinitiator, and a solvent, rendered as a transparent yellow solution. The size distribution of the MAA-NPs is narrow, ranging from 13 to 32 nm with an average diameter of approximately 21 nm (Figure S1, Supporting Information). The MAA functional groups, which are chemically attached to the silica NPs, enhance the dispersibility of NPs in the solvent.[18,25] This effectively minimizes light scattering during femtosecond laser irradiation, thereby achieving submicrometer printing resolution (Figure S2, Supporting Information). Critically, MAA-NPs serve dual roles as photopolymerizable units and silica precursors. With MAA groups, adjacent NPs are directly cross-linked through radical-initiated polymerization upon two-photon excitation[47] (Figure 1b). This reaction is confirmed by the Fourier-transform infrared (FTIR) spectra of the samples before and after printing, where a noticeable decrease in the peak around 1636 cm^{-1} indicates the consumption of C═C bonds during photopolymerization (Figure 1d). The intrinsic cross-linking capability of MAA-NPs eliminates the need for additional photo-cross-linkers,[45,46] which increases the solid content to 78 wt % in our resin (Figure S3, Supporting Information). Due to the absence of photo-cross-linkers, our resin has a simpler composition compared to existing photocurable silica nanocomposites (Table S1, Supporting Information), which makes it low-cost and easily formulated. 4,4′-Bis(diethylamino)-benzophenone is used as a photoinitiator in the resin to achieve TPP printing. With the replacement of the photoinitiator with phenylbis(2,4,6-trimethylbenzoyl)phosphine oxide, the resin can undergo UV curing at 365 nm, allowing for rapid preparation of macroscopic structures (Figure S4, Supporting Information).

During TPP printing, free radicals generated via two-photon absorption initiate localized MAA polymerization that cross-links NPs into dense clusters along the focused laser path.[45,46] This process fabricates 3D microstructures with uniform NP

https://doi.org/10.1021/acsnano.5c09272
ACS Nano 2025, 19, 31643−31655

dispersion and small interparticle spacing, which are essential for ensuring transparency and reducing sintering-induced shrinkage. The printed structure is then developed in ethanol to remove non-cross-linked NPs. Despite the absence of cross-linkers, our strategy still creates mechanically stable microstructures even without supercritical drying. Figure 1b exemplifies a high-quality 3D truss microstructure with 2 μm wide beams, showing no deformation. Moreover, single-arm and four-arm cantilever beams shown in Figure S5 remain fully intact without damage.

Low-Temperature Postprocessing. A moderate sintering temperature of only 650 °C in an air atmosphere is employed in our strategy (Figure S6, Supporting Information). During this process, the polymer chains connecting the NPs are first decomposed, followed by the formation of silicon−oxygen networks between NPs through sintering (Figure 1c). Thermogravimetry-Fourier transform infrared spectroscopy (TG-FTIR)-coupled analysis shows three decomposition stages during heating to 650 °C, with a 22% cumulative mass loss and peaks at 96, 393, and 580 °C (Figures 2a and S3, Supporting Information). The first stage primarily involves the evaporation of trace amounts of residual solvents and physically entrapped water.[48] During the second stage, the observed mass decrement is attributed to thermal degradation of cross-linked and uncross-linked MAA groups, releasing carbon dioxide (CO_2), carbon monoxide (CO), propene (C_3H_6), isobutylene (C_4H_8), and a mixture of acid/carbonyl functionalities.[49] As the decomposition progresses into the third stage, the primary thermal degradation products shift toward CO_2 and CO, indicating the exhaustive oxidation of residual carbonaceous impurities. Beyond 650 °C, the FTIR spectra exhibit no notable alterations, suggesting the cessation of further decomposition and the presence of solely inorganic constituents. Notably, thermogravimetric analysis (TGA) shows a subtle yet persistent mass loss above 650 °C. Considering the absence of carbonaceous impurities, this change is attributed to the dehydroxylation of the material at elevated temperatures.[50] To demonstrate this, the FTIR spectra of the material sintered at different temperatures are collected (Figure 2b). The complete elimination of organic components at 650 °C is evidenced by the absence of peaks at 1640, 1727, and 2960 cm^{-1}, corresponding to the stretching vibrations of C═C, C═O, and C−H, respectively.[51] The broad band centered around 3000−3800 cm^{-1} remains, indicating the presence of physically adsorbed water and residual hydroxyl groups.[51,52] Reheating the 650 °C sintered sample, the TGA result reveals a 0.7% mass loss at approximately 100 °C, corresponding to water evaporation, followed by a slight mass decrease with increasing temperatures, indicating a continuous dehydroxylation process[50] (Figure S7, Supporting Information). Lastly, the FTIR spectrum shows two main peaks at 812 and 1112 cm^{-1}, corresponding to the symmetric and asymmetric stretching vibrations of the Si−O−Si bonds, respectively.[51,52]

The dispersion of NPs has been demonstrated to play a crucial role in high-temperature sintering of high-quality, crack-free glass,[53,54] and similarly, it is vital to the properties of low-temperature sintered glass. The uneven distribution of NPs in conventional nanocomposites leads to the formation of large inorganic vacancies under low-temperature (600 °C) conditions.[20,21] In addition, commonly used NPs have large sizes (≥40 nm), which inherently limits the sintering driving force and leaves most particles unsintered.[41,42] This results in a lower strength of the sintered structure and further exacerbates the formation of large-sized pores. The resulting large and unevenly sized pores cause light scattering, which is the fundamental reason for the low transparency of low-temperature thermally processed nanocomposites. In our strategy, uniform NP distribution achieved through MAA cross-linking avoids possible inorganic vacancies in printed structures, thus eliminating wavelength-scale pores after low-temperature sintering. The enhanced surface energy of 21 nm NPs facilitates viscous flow of amorphous silica NPs at 650 °C, enabling the formation of sintering necks between adjacent particles,[41,42] which further reduces the pore size (Figure 1c). Therefore, uniformly distributed NPs combined with their small size reduce the obstruction of transmitted light by the overall structure. To experimentally prove this, we compare our material with unfunctionalized particle-loaded nanocomposites sintered under identical conditions (Note S1 and Figure S8, Supporting Information). Unfunctionalized particles present poor NP dispersion, resulting in a heterogeneous pore distribution and size. Consequently, the final structure shows low transmittance, regardless of the NP size. By contrast, direct MAA cross-linking in our material ensures optimal NP homogeneity, yielding smoother surfaces and cross sections with better transparency upon sintering at 650 °C. Further high-resolution scanning electron microscopy (SEM) imaging of the internal structure of low-temperature sintered glass reveals that in conventional nanocomposites, most particles remain unsintered with uneven distribution, whereas our material exhibits distinct interparticle sintering and uniformly distributed pores (Figure S9, Supporting Information). The sintered micropattern exhibits high optical transmittance under visible light (Figure 1e). More examples are presented in Figure S10, Supporting Information, where the letters "USTC" are clearly observed even when obscured.

Adhesion between the structure's base and glass substrate induces strain mismatch during heat treatment due to differential shrinkage. The substrate-bound region undergoes constrained shrinkage, whereas the unconstrained upper part shows a greater contraction. The shrinkage gradient causes structural deformation that compromises geometric integrity (Figure S11a, Supporting Information). Although additional sacrificial support or base printing can mitigate distortion, it is not conducive to efficient manufacturing. The fundamental solution to sintering-induced shrinkage deformation lies in minimizing the shrinkage. With small interparticle spacing and restricted particle displacement under low-temperature sintering conditions, our strategy successfully achieves the fabrication of 3D nanoporous glass microstructures with an ultralow shrinkage (Figure 1c). The linear shrinkage rate (SR) is calculated using the formula:

$$\mathrm{SR} = \left(1 - \frac{L'}{L}\right) \times 100\% \tag{1}$$

where L represents the postprinting dimension and L' represents the postsintering dimension (Figure S11b, Supporting Information). Ultimately, the 3D architecture demonstrates only ∼5% linear shrinkage during the entire heating process (Table S2, Supporting Information), which makes strain mismatch negligible without additional steps. The macroscopic sample also exhibits a linear shrinkage rate as low as 4.94% (Figure S12, Supporting Information). Additionally, the shrinkage rate for the as-printed material in comparison to

https://doi.org/10.1021/acsnano.5c09272
ACS Nano 2025, 19, 31643−31655

the printing design is approximately 1.34% (Table S2, Supporting Information). To increase the reliability of shrinkage assessment, we measure the linear shrinkage rate of a 20 μm diameter sphere,[55] which can better represent actual optical elements. The shrinkage is measured to be 4.96%, which is basically consistent with the shrinkage assessment of the 3D microstructure (Figure S13, Supporting Information). To emphasize the pivotal role of the cross-linker-free material system in minimizing shrinkage, we incorporate varying concentrations of pentaerythritol triacrylate (PETA) into the resin. The results show a positive correlation between the shrinkage rate and PETA content, demonstrating that the densely packed initial arrangement of NPs effectively minimizes dimensional reduction (Figure S14, Supporting Information). Compared with conventional high-shrinkage systems, minimal shrinkage reduces deformation and eliminates the need for sacrificial support, thereby improving shape fidelity and manufacturing efficiency.

To be more intuitive, our strategy is compared with other reported strategies in terms of processing temperature and shrinkage rate (Figure 1f and Table S3, Supporting Information). For NP-loaded resins, achieving transparency of the silica structure typically requires temperatures exceeding 1000 °C, often approaching 1300 °C. The sole exception is the one-photon microstereolithography (OμSL) technology,[18] which employs the similarity−interchangeability theory to create a nanocomposite ink with exceptionally uniform NP dispersion. Although not detailed in their work, this material shows transparency after 600 °C pyrolysis, which corroborates our hypothesis that small, uniformly dispersed NPs enable low-temperature transparency. However, its shrinkage rate is high due to the presence of a large amount of organic components, which increases interparticle spacing. Conversely, NP-free resins require lower processing temperatures but reveal higher shrinkage rates. Hydrogen silsesquioxane (HSQ), while capable of directly printing nearly carbon-free silica and indistinguishable from silica glass after annealing at 900 °C with 6.1% linear shrinkage,[34] is impractical for efficient manufacturing due to its 1 μm s^{-1} printing speed. Our strategy offers an excellent balance between transparency, processing temperature, and shrinkage rate. Moreover, it is worth noting that our material can achieve transparent structures over a broad temperature range (650−1050 °C). At the same temperature, the shrinkage rate of our material is generally minimal, even when it is fully sintered at 1050 °C.

Material Characterization. A series of material characterizations is conducted to verify the chemical composition and physical characteristics of the low-temperature sintered nanoporous glass. Raman spectroscopy measurements are performed to characterize the material's structural properties (Figure 2c). As a reference, the spectrum of a commercial fused silica glass slice (JGS-2 grade, SiO_2 ≥99.9999%) is provided. Comparative analysis shows that all organic spectral features are completely eliminated, thereby confirming the results obtained from FTIR spectroscopy. The sintered nanoporous glass exhibits a Raman spectrum similar to that of the commercial reference. The ω_1 and ω_3 bands correspond to the bending vibration of the $Si(O_{1/2})_4$ tetrahedrons' Si−O−Si bridges, and the ω_4 bands are ascribed to the stretching motion of the Si−O bonds. The D_1 and D_2 lines correspond to the symmetric stretching of silicon−oxygen ring molecules.[28,56] The differences in the intensity are explained by the inherent structural disparities in silica-membered rings.[57] The emergence of an additional peak at 982 cm^{-1} and a distinct band within the 3000−3800 cm^{-1} region indicates the presence of Si−OH within the structure,[58] which can be eliminated after sintering at 1050 °C (Figure S15, Supporting Information).

The elemental composition is measured by the X-ray photoelectron spectroscopy (XPS) analysis (0−1200 eV, Figure 2d). As expected, the 650 °C sintered structure is mainly composed of silicon and oxygen (Si: 34.83%, O: 63.12%, C: 2.05%; Table S4, Supporting Information), which aligns with the elemental composition of commercially available fused silica glass (Si: 34.54%, O: 63.65%, C: 1.80%; Table S4, Supporting Information). The minor carbon content is attributed to adventitious carbon contamination during testing, which is usually employed for XPS calibration. In the fine spectroscopy results, the peaks of the sintered glass match very well with commercial specimens (532.6 eV for O 1s peak, 103.4 eV for Si 2p peak, and 25.3 eV for O 2s peak), which indicates their identical chemical state and structural composition (Figure S16, Supporting Information).

TEM is used to record internal structure evolution intuitively (Figure 2e). The tested TEM samples are sliced from 400 and 650 °C sintered glass microstructures via focused ion beam cutting. Bright-field TEM imaging at 400 °C shows densely packed discrete NPs, indicating that NP sintering did not occur at this temperature. In contrast, at 650 °C, the formation of sintering necks between particles confirms that sintering has taken place. This phenomenon strongly confirms the feasibility of sintering at 650 °C. The final sintered structure exhibits a uniformly distributed nanoporous internal characteristic. To further quantitatively assess pore characteristics, N_2 adsorption−desorption measurement is performed on the sintered macroscopic structure. Barrett−Joyner−Halenda (BJH) analysis of the desorption branch exhibits an average pore size of 6.65 nm (Figure S17, Supporting Information), aligning with TEM observations. The homogeneous nanoscale porosity accounts for the retained optical transparency despite low-temperature processing.[37] The density of the sintered nanoporous glass, which is measured to be 1.24 g cm^{-3}, is lower than that of fused silica glass (2.20 g cm^{-3}) due to its porous nature (Note S2, Figure S18, and Table S5, Supporting Information). Further heating induces progressive structural shrinkage, and the shrinkage rate sharply increases above 1000 °C due to the collapse of nanopores (Figure S19, Supporting Information). After sintering at 1050 °C, the structure becomes completely dense (Figure S20, Supporting Information). Despite its inherent porosity, the nanoporous glass exhibits robust mechanical properties. In situ compression testing of a 650 °C sintered micropillar displays elastic−plastic deformation with a compressive strength exceeding 2 GPa (Figure 2f). This value is lower than the value after complete sintering at 1050 °C (Figure S21, Supporting Information) due to the presence of nanopores but still surpasses the strength of most state-of-the-art polymers.[59] Figure 2f also highlights a significant enhancement in the mechanical properties of the sintered silica compared to the printed microstructure, which provides additional evidence of sintering between NPs. The Young's modulus, thermal expansion, and laser damage threshold of the nanoporous glass are discussed in Note S3 and Figures S22, S23, Supporting Information. Additionally, an energy-dispersive spectroscopy test demonstrates the homogeneous distributions of Si and O elements (Figure S24, Supporting Information). Selected-area electron diffraction (SAED) pattern and X-ray diffraction

https://doi.org/10.1021/acsnano.5c09272
ACS Nano 2025, 19, 31643−31655

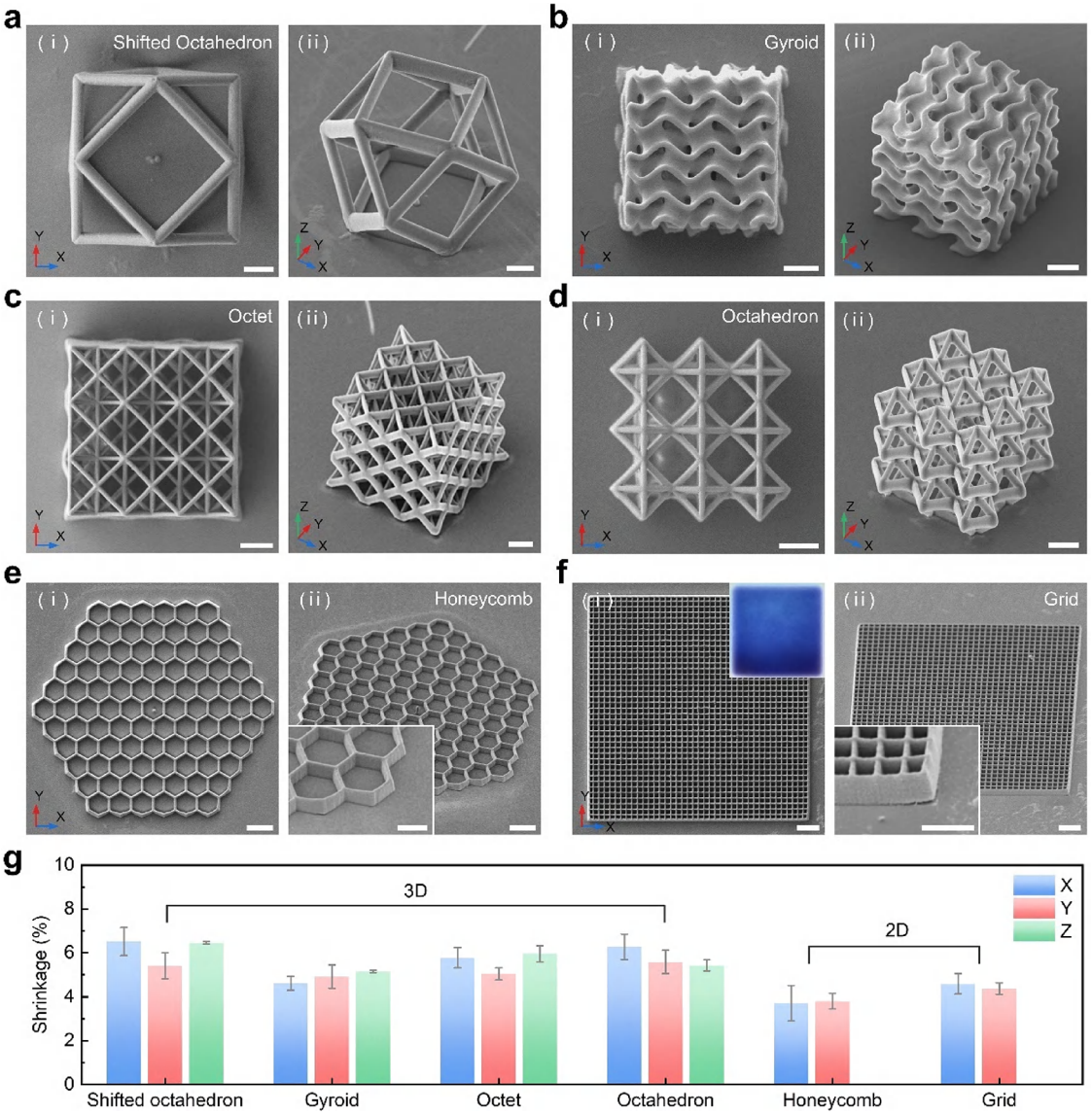

Figure 3. High-fidelity 3D nanoporous glass microstructures. (a–d) SEM images of various complex 3D glass microstructures, including (a) unit shifted octahedron, (b) gyroid structure with a triply periodic minimal surface, (c) 3 × 3 × 3 octet microlattice, and (d) 3 × 3 × 3 octahedron microlattice. All microstructures show high uniformity and fidelity. Scale bars, 10 μm. (e, f) SEM images of 2D glass microstructures, including (e) honeycomb structure and (f) grid structure with a rod width of 600 nm. The enlarged SEM images show no edge delamination and curling. The grid structure exhibits a blue structural coloration under transmitted light illumination. Scale bars, 10 and 5 μm for enlarged SEM images. (g) Measured shrinkage rates of the fabricated glass microstructures.

(XRD) results collectively verify the amorphous phase of the sintered glass (Figure S25, Supporting Information).

High-Fidelity 3D Nanoporous Glass Microstructures. To demonstrate the robustness of our strategy, a series of complex 3D nanoporous glass microstructures with high fidelity and precision are fabricated. All structures undergo identical low-temperature heat treatment. Notably, a unit shifted octahedron, a gyroid structure with a triply periodic minimal surface, a 3 × 3 × 3 octet microlattice, and a 3 × 3 × 3 octahedron microlattice are successfully fabricated (Figure 3a–d). These examples highlight the exceptional manufacturing capability of our strategy and its potential for the creation of mechanical metamaterials. The minimal shrinkage ensures negligible strain mismatch even without sacrificial support and promotes the successful fabrication of crack-free silica microstructures with high uniformity and fidelity. Two-dimensional (2D) honeycomb and grid structures are further printed directly on substrates, with lateral dimensions of 100 μm × 100 μm and a height of 3 μm (Figure 3e,f). Such thin architectures are highly susceptible to edge delamination and curling due to substrate-induced strain gradients, which pose significant challenges for resins with high shrinkage rates. However, our strategy eliminates these defects, preserving the structural integrity after sintering. Owing to the high-resolution TPP fabrication, the grid structure with submicron feature size (rod width: 600 nm) exhibits blue structural coloration under transmitted light illumination (Figures 3f and S26, Supporting Information).

To measure the shrinkage rates of these microstructures, the microstructures before sintering are characterized, as shown in Figure S27, Supporting Information. The results show that all microstructures have low shrinkage rates (Figure 3g). The longitudinal dimensions of the 2D microstructures show significant measurement errors due to the randomness of the

https://doi.org/10.1021/acsnano.5c09272
ACS Nano 2025, 19, 31643–31655

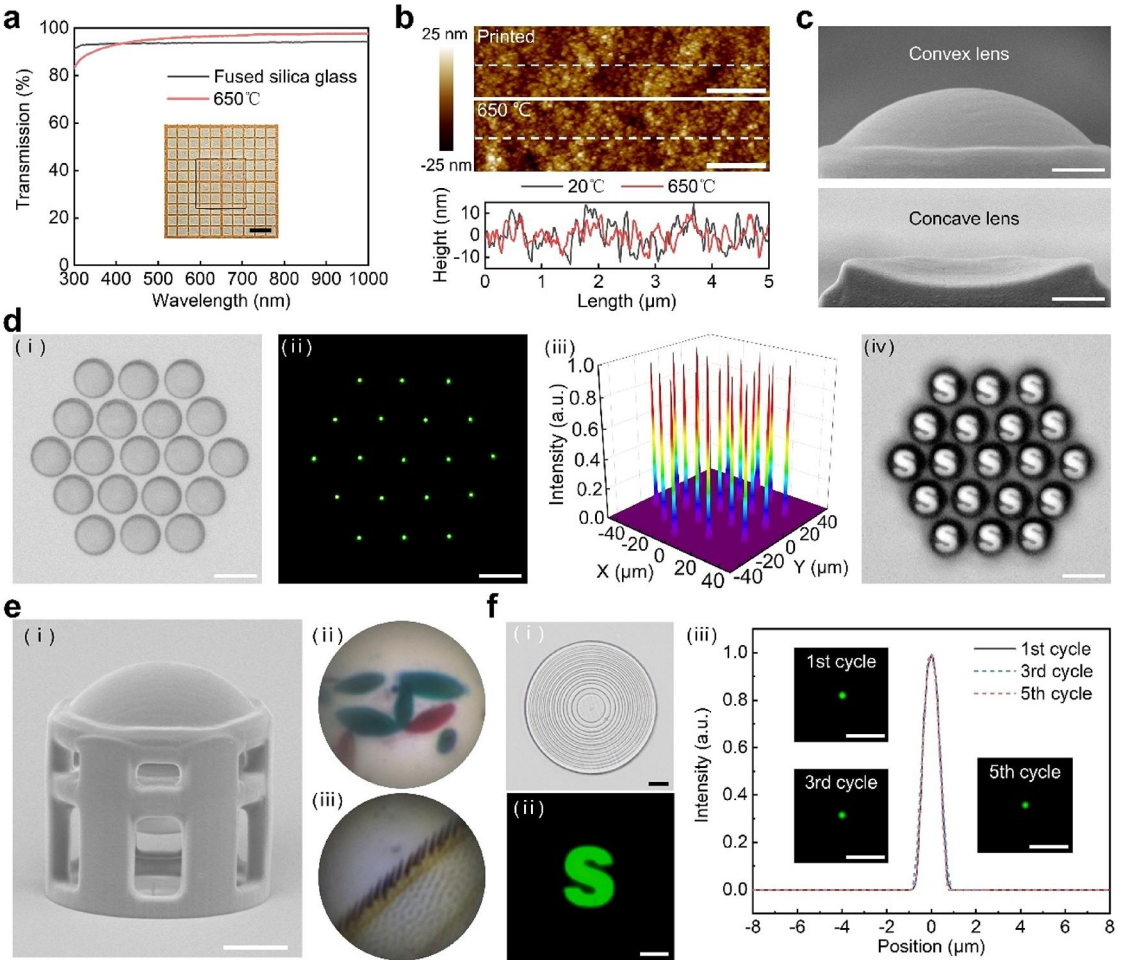

Figure 4. 3D glass micro-optics. (a) Optical transmission comparison between the 650 °C sintered nanoporous glass and commercial fused silica glass. The inset shows the 200 μm thick unpolished block used for measurement. Scale bar, 2 mm. (b) AFM measurements of the printed and 650 °C sintered microblocks, demonstrating low surface roughness. Scale bars, 1 μm. (c) Fabricated glass convex and concave microlens. Scale bars, 10 μm. (d) Characterization of the glass hexagonal microlens array, including (i) optical image, (ii) focused light spot, (iii) normalized light density distribution, and (iv) imaging of the letter "S". Scale bars, 20 μm. (e) Characterization of the ultracompact doublet microlens, including (i) SEM image and (ii-iii) imaging of Paramecia and Drosophila. Scale bar: 20 μm. (f) Characterization of the glass FZP, including (i) optical image and (ii) imaging of the letter "S". (iii) FWHM of optical intensity profiles and the focused light spots (the inset) remains almost unchanged after multiple cycles of 600 °C annealing. Scale bars: (i) 10 μm and (ii-iii) 5 μm.

initial plane selection for TPP printing; therefore, only the changes in lateral dimensions are recorded. Compared with 3D geometries, 2D planar structures are more easily constrained by the substrate due to their smaller longitudinal dimensions, resulting in a smaller shrinkage rate. Overall, we achieve a method of printing distortion-free transparent 3D nanoporous glass microstructures without the need for additional supports or bases, which is particularly challenging for processes with high shrinkage. Our strategy is expected to facilitate the development and widespread application of mechanical metamaterials with lightweight and high-strength properties.[60]

Glass Micro-Optics. To investigate the optical properties of low-temperature sintered nanoporous glass, we measure the ultraviolet−visible−near-infrared (UV−Vis−NIR) transmission spectrum of a 200 μm thick unpolished block fabricated through UV curing and 650 °C sintering (Figure 4a). Commercial silica glass with the same thickness is used as a reference. Due to the presence of nanopores, nanoporous glass has a lower refractive index compared to commercial fused silica glass, which means that nanoporous glass has lower interfacial reflection losses[61,62] (Note S4, Note S5, and Figure S28, Supporting Information). Meanwhile, the subwavelength scale of these nanopores minimizes light scattering (Note S5, Supporting Information). As a result, the fabricated nanoporous glass has good optical visible light transmittance (97%), which is in sharp contrast to opaque conventional low-temperature sintered nanocomposites. While nanoporosity reduces ultraviolet transmittance relative to commercial fused silica glass, no distinct absorption cutoff edge is observed. The thickness has a greater impact on the transmittance of nanoporous glass; however, for structures not exceeding 1 mm, the transmittance remains at a relatively high value (Figure S29, Supporting Information). Atomic force microscopy (AFM) measurements on a sintered microblock show an arithmetic mean line roughness (Ra) of 5.5 nm, representing an improvement compared to the as-printed part (Figure 4b). Despite being slightly higher than reported values for high-temperature annealed nanocomposites, the roughness meets the requirement of glass micro-optics. Further annealing at 1050 °C reduces Ra to 2.6 nm (Figure S30, Supporting Information), enabling the direct fabrication of optical-grade freeform lenses. Figure 4c displays the side profiles of the

https://doi.org/10.1021/acsnano.5c09272
ACS Nano 2025, 19, 31643−31655

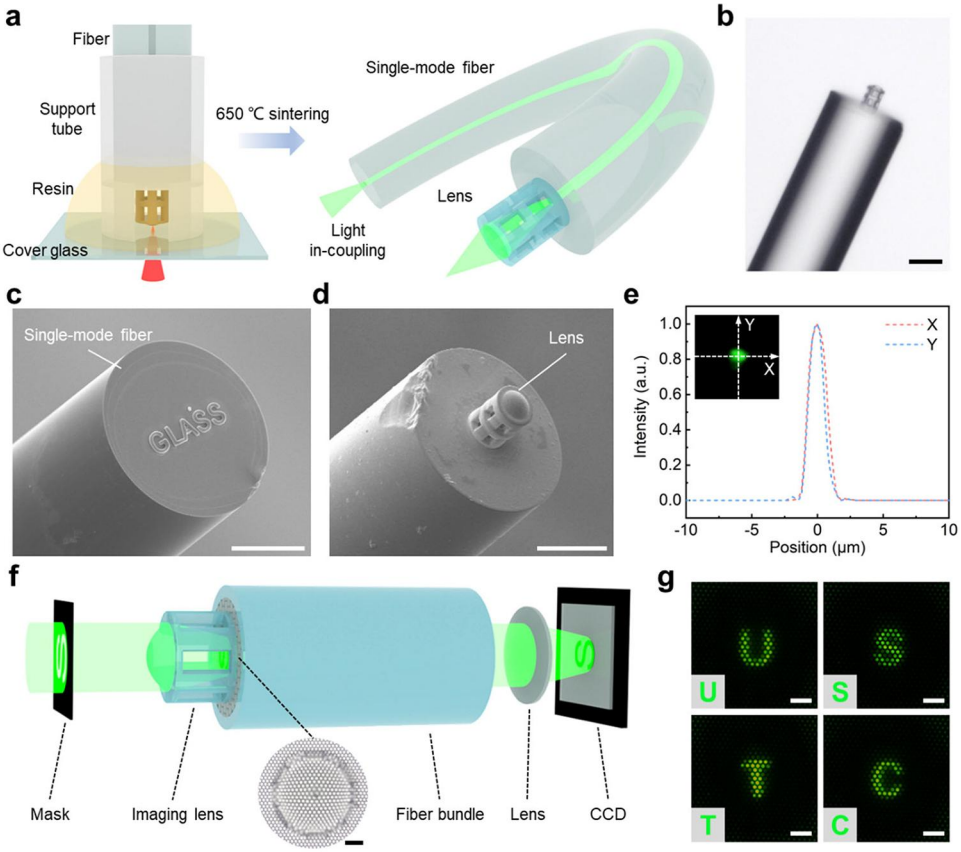

Figure 5. Optical fiber integration with glass microlens. (a) Schematic illustration of the no assembly, integrated manufacturing process for fabricating an all-glass "lens-on-fiber" device. (b) Optical image of the integrated device. Scale bar, 50 μm. (c) Silica microword "GLASS" printed on the end face of an optical fiber, showing no deformation. Scale bar: 50 μm. (d) Fabricated "lens-on-fiber" device, showing minimal deviation of the lens after sintering. Scale bar, 50 μm. (e) FWHM of the focused spot, obtained by coupling a 550 nm laser into the fiber and focusing it through the glass lens. The focused spot exhibits slight differences in both the X and Y directions, demonstrating good alignment. (f) Schematic diagram of the glass microendoscopy imaging system. Scale bar: 20 μm. (g) Imaging of the letters "U", "S", "T", and "C". Scale bars, 20 μm.

fabricated convex and concave lenses, with the latter partially fabricated for ease of observation. We characterize the broadband focusing performance of the convex lens by collecting cross sections of optical intensity along the optical axis plane at various wavelengths. The measured axial focal positions remain nearly identical for wavelengths of 470, 550, and 620 nm, confirming the low chromatic aberration of the microlens (Figure S31, Supporting Information). Moreover, our microlenses offer significant cost advantages over current 3D-printed glass microlenses, mainly due to reduced material costs and lower energy consumption. The unique low-shrinkage characteristic enables our microlenses to maintain structural integrity during sintering without requiring sacrificial bases, thus reducing design complexity and processing time.

To further demonstrate the capability of our low-temperature sintering strategy for fabricating micro-optics, we fabricate a variety of such microdevices. A microlens array (MLA) consisting of multiple individual microlenses arranged in a certain order enables advanced functionalities such as wavefront detection[63] and beam homogenization.[64] To maximize the light collection efficiency of an MLA, a high fill factor is a crucial requirement.[65] By using our strategy, a hexagonal MLA with a 90.69% theoretical maximum fill factor can be printed directly on a fused silica substrate [Figure 4d(i)]. Benefiting from ∼5% linear shrinkage, the postsintered MLA maintains a high fill factor (81.85%), which enhances light utilization efficiency (Note S6 and Figure S32, Supporting Information). The uniform light intensity distribution [Figure 4d(ii-iii) and Figure S33, Supporting Information] and distortion-free imaging of the letter "S" [Figure 4d(iv)] confirm good optical performance, which matches that of microlenses fabricated via traditional manufacturing techniques.[66] Line-focusing cylindrical lenses are similarly demonstrated (Figure S34 in the Supporting Information). We further fabricated an ultracompact glass doublet lens and exhibited the imaging results of Paramecia and Drosophila (Figure 4e). Such a complex microlens is difficult to fabricate using traditional methods, such as subtractive top-down approaches.[66] Additional microlens is fabricated using the organic−inorganic hybrid photoresist SZ2080 for comparative imaging evaluation. Both systems demonstrate comparable imaging performance (Figure S35 in the Supporting Information).

Our strategy enables the fabrication of distortion-free binary diffractive optical elements. As proof, a glass Fresnel zone plate (FZP) comprising 10 concentric rings is constructed (Figure 4f(i)). Notably, the narrowest ring width in the FZP reaches 650 nm (Figure S36, Supporting Information). Under illumination at a wavelength of 550 nm, the FZP produces a round focal spot through optical diffraction, with 0.76 μm full width at half-maximum (FWHM), indicating good focusing performance. Excellent imaging characteristics are also

https://doi.org/10.1021/acsnano.5c09272
ACS Nano 2025, 19, 31643−31655

obtained, as observed in Figure 4f(ii). The thermal and chemical resistance of the nanoporous glass device is further demonstrated by evaluating the focusing feature after thermal and chemical treatment. By subjecting to 5 cycles of 600 °C annealing, the FWHM of optical intensity profiles remains almost unchanged (Figure 4f(iii)). After the FZP was soaked in various representative chemical reagents for 1 h, negligible changes in the focusing feature were observed (Figure S37, Supporting Information). The good thermal and chemical resistances of low-temperature sintered glass promote the wide applications of optics in extreme thermal and corrosive environments.

Glass "Lens-on-Fiber" Microdevices. Based on the proposed strategy, we integrate micro-optics onto optical fiber end facets to demonstrate the potential application prospects of our strategy in microsystem integration. Optical fiber-integrated microdevices, which integrate 3D micro-optics with optical fibers, hold promising applications in beam shaping,[10] laser manufacturing,[11] and endoscopic imaging.[12,13] Currently, microdevices on optical fibers are primarily made of organic polymers, which suffer from limited thermal stability and low laser damage thresholds. Glass materials are expected to overcome these problems, especially with their good biocompatibility, which makes them promising for biomedical applications.[67,68] However, conventional glass fabrication methods face challenges due to high-temperature processing constraints[30,35] and structural misalignment caused by excessive shrinkage. The real solution to this challenge lies in developing an ink that can be used "as-printed" and does not require sintering; however, such research is still in its early stage.[33,34] Currently, thermal-processing-based techniques remain the mainstream methods for glass manufacturing. Here, our low-temperature, low-shrinkage 3D printing strategy enables direct integration of glass micro-optics onto optical fibers (without cladding polymer) with high alignment precision. As a proof of concept, we fabricate an all-glass "lens-on-fiber" device by directly printing a microlens onto a fiber end facet without assembly steps (Figure 5a). After sintering in air at 650 °C, both the lens and the fiber maintain optical transparency (Figure 5b). Figure 5c displays the SEM image of the silica microword "GLASS" printed on the end face of an optical fiber, demonstrating that the structure experiences minimal deformation during sintering. Low shrinkage minimizes the deviation of the lens after sintering, ensuring efficient light coupling (Figure 5d). To demonstrate this, a 550 nm laser is coupled into the fiber and focused by the glass lens upon emerging from the end. The FWHM of the focused spot exhibits slight differences in the X and Y directions, demonstrating precise lens-fiber alignment (Figure 5e). Additional integrated glass microstructures are shown in Figure S38, Supporting Information. We further develop a glass microendoscopy system by integrating an 80 μm diameter microlens onto a fiber bundle. This system projects the images of objects onto the fiber bundles' distal end, transmitting them to the proximal end for capture via a 50× objective and charge-coupled device (CCD) camera (Figure 5f). Consequently, the letters "U", "S", "T", and "C" are imaged (Figure 5g). This approach holds promise for integrating more complex glass optical systems onto optical fibers and provides a scalable platform for multifunctional optical fiber systems in biomedical imaging and industrial laser applications.

CONCLUSIONS

To obtain transparent glass, particle-based glass 3D printing typically requires high-temperature sintering for full densification, causing significant structural shrinkage. In this work, a low-temperature, low-shrinkage 3D printing strategy is developed to fabricate transparent nanoporous glass microstructures using particle-loaded resins. The crucial innovation of our strategy lies in the MAA-NPs-loaded resin, which, unlike conventional nanocomposites, does not require cross-linkers. Through MAA cross-linking, small NPs are densely and uniformly arranged in the printed structures. This innovation led to two major advances. First, we experimentally confirm that NP sintering initiates at 650 °C, leveraging the small particle size (21 nm). Unlike conventional nanocomposites that form large, unevenly distributed pores after low-temperature processing,[20,21] our approach, benefiting from the initial densely packed NP arrangement, yields nanoporous glass with small (6.65 nm), uniformly distributed pores after low-temperature sintering. This nanostructure significantly reduces light scattering, thereby achieving high transparency in the sintered structures. This advancement challenges the long-held notion that particle-based nanocomposites require ultrahigh temperatures to produce transparent glass, positioning our particle-loaded system within the emerging paradigm of low-temperature glass fabrication. Second, due to the restricted particle displacement during low-temperature sintering and the initial dense particle packing, our printed 3D microstructures exhibit a uniform shrinkage rate of ∼5%, much lower than most reported glass 3D printing technologies.[23,25,28] Consequently, unlike existing methods that require sacrificial bases to preserve structural integrity, our strategy achieves high shape fidelity in 3D glass microarchitectures without additional processing steps. Building on these dual advancements, we successfully fabricated glass "lens-on-fiber" microdevices with high alignment precision through direct in situ integration, eliminating the assembly steps. The nanoporous glass produced by our strategy also holds potential for applications such as photofunctionalization,[37,69] antireflective coatings,[61,62] and drug delivery systems.[70] Overall, this work highlights an attractive combination of low thermal processing temperature, high transmittance, and minimal shrinkage for 3D glass manufacturing, offering broad application prospects ranging from micro-optics, photonics, and biomedical microdevices to integrated microsystems.

EXPERIMENTAL SECTION

Materials. A solution of propylene glycol monomethyl ether containing homogeneously dispersed methacrylic acid-functionalized silica nanoparticles (MAA-NPs, SiO_2 content ∼40 wt %) was purchased as a catalog product from Shanghai Jiute Nanomaterial Technology Co., Ltd. 4,4′-Bis (diethylamino) benzophenone (EMK, ≥99%) was purchased from Aladdin. Phenylbis (2,4,6-trimethylbenzoyl) phosphine oxide (XBPO, 98%) and pentaerythritol triacrylate (PETA, 96%) were purchased from Macklin. Ethanol (≥99.5%), ethylene glycol (≥99.5%), methanol (≥99.5%), isopropanol (≥99.7%), 1-propanol (≥99.5%), hydrochloric acid (36.0−38.0%), and sodium hydroxide (≥96.0%) were purchased from Sinopharm Chemical Reagent Co., Ltd. Fused silica glass slides (25 mm × 25 mm × 0.2 mm) were purchased from Donghai Jinpute Optoelectronics Technology Co., Ltd.

Resin Preparation. The resin only consists of MAA-NPs, a photoinitiator, and a small amount of solvent. First, 5 g of functionalized silica NP solution is heated to 65 °C for 20 h in an oven to evaporate 2.3 g of the solvent. Then, for the TPP printing

https://doi.org/10.1021/acsnano.5c09272
ACS Nano 2025, 19, 31643−31655

precursor, 40 mg of EMK (acting as a photoinitiator) is directly mixed with the solution, followed by ultrasonic treatment until the resulting solution becomes completely transparent. For the UV printing precursor, 20 mg of XBPO is used as the photoinitiator, and the remaining steps are the same.

Fabrication of 3D Microstructures. The resin is printed by a homemade TPP printing system. The femtosecond laser source is a mode-locked Ti: sapphire ultrafast oscillator (Chameleon Vision-S, Coherent Crop, central wavelength: 800 nm, pulse width: 75 fs, repetition rate: 80 MHz). The laser is tightly focused by a 60× oil-immersion objective with high numerical aperture (NA = 1.35) in order to realize high resolution. The laser focus is steered by a pair of galvomirrors for 2D scanning, while the step between layers is realized by linear nanopositioning. Before printing, 20 μL of the resin is dropped onto a fused silica glass slide (thickness: 200 μm) and baked on a hot plate at 100 °C for 90 s to remove as much excess solvent as possible. Point-by-point scanning paths are generated from the home-built slicing software according to the designed 3D models, in which the slicing distance and hatching distance are all set to 100−300 nm. The laser power and scanning speed are set to 10−30 mW and 50−400 μm s^{-1}, respectively. After printing, the sample is immersed in ethanol for 30 min to remove the uncured part. The sample is then dried under ambient conditions without additional operations. The heat treatment processes for all samples are conducted in a muffle furnace (KSL-1500X, HF-kejing, China) in air. During the process, the temperature is increased to the target temperature at a ramping-up rate of 1 °C min^{-1}. The dwelling times are, respectively, set as 120, 180, and 600 min when the temperature reaches 200, 400, and 650 °C, respectively. After that, the samples are gradually cooled to room temperature at a ramping-down rate of 2 °C min^{-1}.

Fabrication of 3D Microstructures on Fiber. First, a homemade support tube is used to hold the optical fiber in a vertical orientation and maintain a gap between the fiber end facet and the cover glass of ≈120 μm. Before being held, the cladding polymer on the optical fiber is removed. Next, 20 μL of resin is dropped on the glass substrate to wrap the fiber tip and baked at 100 °C for 90 s to evaporate the solvent in the resin. Then, the fiber is suspended with the tip facing downward toward the focal plane of the processing system. The position of the fiber is adjusted according to a magnified CCD image under transmitted light illumination. After that, the designed microstructure is directly printed on the fiber end facet by TPP. After polymerization, the sample is developed in ethanol for 30 min until all the uncured part is removed. Finally, the fiber is transferred to a muffle furnace for sintering, resulting in glass "lens-on-fiber" microdevices.

Morphological Characterization. SEM images are taken with a secondary-electron scanning electron microscope (EVO18, ZEISS) operating at an acceleration voltage of 10 keV after depositing ∼10 nm gold. TEM images of the MAA-NPs are obtained by a high-resolution transmission electron microscope (HT7700 Exalens, HITACHI) operating at an acceleration voltage of 200 kV. TEM characterizations of sintered glass are done with a field emission transmission electron microscope (JEM-2100F, JEOL) operating at an acceleration voltage of 200 kV. The tested TEM samples are sliced from sintered silica glass microstructures via focused ion beam (FIB, FEI Helios NanoLab650, Thermo Fisher Scientific) cutting. The surface roughness is measured using an AFM system (Dimension Icon, Bruker).

Chemical and Compositional Characterization. To facilitate experimental procedures, some tests are conducted using UV-cured macroscopic samples. The impact of different printing methods on the final material's properties is explained in Note S7, Supporting Information. TG-FTIR is performed by a combination of a thermogravimetric analyzer (TGA-8000, PerkinElmer) and a Fourier transform infrared spectrometer (Frontier, PerkinElmer). TGA is performed with the temperature gradually increased to a maximum temperature of 1000 °C at a rate of 10 °C min^{-1}. FTIR analyses of sintered samples are conducted by a Fourier transform infrared spectrometer (Thermo Nicolet iS5, Thermo Fisher Scientific). Raman spectra are acquired from a Raman spectrometer (LabRam HR Evolution, HORIBA Scientific) under 532 nm excitation. XRD analyses are performed on a theta−theta rotating anode X-ray diffractometer (TTR-III, Rigaku). The tested samples used above are macroscopic and were obtained through UV curing. XPS data are analyzed using an in situ X-ray photoelectron spectrometer (ESCALAB 250Xi, Thermo Fisher Scientific).

Mechanical and Physical Characterization. In situ compression tests are conducted by a KLA NanoFlip Nanoindenter with a diamond flat punch tip with a diameter of 10 μm in a ZEISS Gemini SEM 360. The compression tests are performed at a displacement rate of 10 nm s^{-1} for all micropillars. The force signals are acquired through a pressure transducer. The pore size distribution is measured with the use of an N_2 adsorption−desorption apparatus (Micromeritics ASAP 2460) at −196 °C. The tested sample is obtained through UV curing and sintering, followed by degassing under vacuum at 120 °C for 6 h before the analysis. The pore size distribution is calculated by Barrett−Joyner−Halenda (BJH) equations, over the acquired adsorption data points. The density of the obtained nanoporous silica glass is calculated by measuring the mass and volume of a thin-film sample (Note S2, Supporting Information).

Optical Characterization. The optical microscopy images are obtained using an inverted microscope (DMI 3000B, Leica). Optical transmission is characterized using a UV−Vis−NIR spectrometer (SolidSpec-3700i, Shimadzu). The tested sample is obtained through UV curing and sintering to match the thickness of commercial silica glass used as a reference. Refractive indices are measured using ellipsometry on UV-cured and sintered macroscopic films. The focusing characteristics of the microlenses are measured by the microscope. The 2D images of focused light spots are captured using a CCD camera.

ASSOCIATED CONTENT

Supporting Information

The Supporting Information is available free of charge at https://pubs.acs.org/doi/10.1021/acsnano.5c09272.

Supplementary notes; size characterization of silica nanoparticles; evaluation of the print resolution of the resin; TGA of the cured resin; UV−visible absorption spectra and molecular structures of photoinitiators for different printing methods; evaluation of print stability; heating procedure; TGA of the 650 °C sintered glass; comparison of 650 °C sintered macroscopic bulk silica; high-resolution SEM images of the interior structures of 650 °C sintered macroscopic bulk silica; optical microscopy images of the sintered silica micropattern; measurement and comparison of the shrinkage rate of 3D microstructures; shrinkage rate of macroscopic samples; shrinkage rate of a 20 μm diameter sphere; measurement of the shrinkage rate of 3D microtruss with increasing PETA contents; Raman spectra of 1050 °C sintered silica; fine XPS spectra of low-temperature sintered glass and fused silica glass; N_2 adsorption−desorption measurement of low-temperature sintered glass; measurement of the density of macroscopic samples; shrinkage rate of 3D microtruss with increasing temperatures; bright-field TEM images and a selected-area diffraction pattern of the 1050 °C sintered glass; mechanical properties of the 1050 °C sintered structure; nanoindentation characterization of the 650 and 1050 °C sintered glass; characterization of laser damage resistance of 650 and 1050 °C sintered glass; FIB-TEM characterization of low-temperature sintered glass; selected-area electron diffraction pattern and X-ray diffraction spectrum of low-temperature sintered glass; 2D grid structures with different structural parameters;

https://doi.org/10.1021/acsnano.5c09272
ACS Nano 2025, 19, 31643−31655

printed 3D microstructures; refractive and loss coefficient of low-temperature sintered glass; optical transmission of the 650 °C sintered nanoporous glass and commercial fused silica glass with different thicknesses; effect of annealing temperature on structural roughness; experimental characterization of low dispersion behavior of low-temperature sintered glass microlens; schematic diagram of the change in the fill factor of the MLA after sintering; optical properties of low-temperature sintered glass MLA; characterization of low-temperature sintered glass cylindrical microlens; comparison of imaging between sintered glass microlens and microlens fabricated using SZ2080; SEM images of glass FZP; evaluation of chemical resistance of the glass FZP; glass microstructure printed and sintered on the end face of optical fiber; comparison of the composition of existing photocurable silica nanocomposites and our resin; shrinkage rate in different directions of microstructures fabricated by our resin; comparison of our proposed approach and the reported transparent glass 3D printing techniques with different materials in terms of processing temperature and shrinkage rate; elemental composition analyzed from the XPS results of printed, 650 °C sintered, and commercially available fused silica glass; and density of the obtained nanoporous glass (PDF)

AUTHOR INFORMATION

Corresponding Author

Jiawen Li − *CAS Key Laboratory of Mechanical Behavior and Design of Materials, Key Laboratory of Precision Scientific Instrumentation of Anhui Higher Education Institutes, Department of Precision Machinery and Precision Instrumentation, University of Science and Technology of China, Hefei 230027, China;* orcid.org/0000-0003-3950-6212; Email: jwl@ustc.edu.cn

Authors

Yuan Tao − *CAS Key Laboratory of Mechanical Behavior and Design of Materials, Key Laboratory of Precision Scientific Instrumentation of Anhui Higher Education Institutes, Department of Precision Machinery and Precision Instrumentation, University of Science and Technology of China, Hefei 230027, China*

Xinyi Gu − *CAS Key Laboratory of Mechanical Behavior and Design of Materials, Key Laboratory of Precision Scientific Instrumentation of Anhui Higher Education Institutes, Department of Precision Machinery and Precision Instrumentation, University of Science and Technology of China, Hefei 230027, China*

Hao Wu − *School of Microelectronics, Hefei University of Technology, Hefei 230601, China*

Jincheng Ni − *CAS Key Laboratory of Mechanical Behavior and Design of Materials, Key Laboratory of Precision Scientific Instrumentation of Anhui Higher Education Institutes, Department of Precision Machinery and Precision Instrumentation, University of Science and Technology of China, Hefei 230027, China*

Yanlei Hu − *CAS Key Laboratory of Mechanical Behavior and Design of Materials, Key Laboratory of Precision Scientific Instrumentation of Anhui Higher Education Institutes, Department of Precision Machinery and Precision Instrumentation, University of Science and Technology of China, Hefei 230027, China;* orcid.org/0000-0003-1964-0043

Dong Wu − *CAS Key Laboratory of Mechanical Behavior and Design of Materials, Key Laboratory of Precision Scientific Instrumentation of Anhui Higher Education Institutes, Department of Precision Machinery and Precision Instrumentation, University of Science and Technology of China, Hefei 230027, China;* orcid.org/0000-0003-0623-1515

Jiaru Chu − *CAS Key Laboratory of Mechanical Behavior and Design of Materials, Key Laboratory of Precision Scientific Instrumentation of Anhui Higher Education Institutes, Department of Precision Machinery and Precision Instrumentation, University of Science and Technology of China, Hefei 230027, China;* orcid.org/0000-0001-6472-8103

Complete contact information is available at: https://pubs.acs.org/10.1021/acsnano.5c09272

Author Contributions

Y.T. and J.L. conceived the idea and designed the project. J.L. supervised the project. Y.T. performed all the experiments and the characterization. Y.T., J.N., Y.H., D.W., J.C., and J.L. completed data analysis and figure depicture. Y.T. and J.L. wrote the paper. Y.T., X.G., H.W., and J.L. revised the paper. All the authors discussed the results and made recommendations.

Notes

The authors declare no competing financial interest.

ACKNOWLEDGMENTS

This work was supported by the National Natural Science Foundation of China (Nos. 52075516, 62325507, 62375253, 52375582), the National Key Research and Development Program of China (Nos. 2021YFF0502700, 2024YFB4610700), the Hefei Municipal Natural Science Foundation (No. HZR2450), the National Synchrotron Radiation Laboratory (KY2090000143), the Major Scientific and Technological Projects in Anhui Province (202103a05020005, 202203a05020014), the Anhui Provincial Natural Science Foundation (2308085QF218), the Fundamental Research Funds for the Central Universities (WK2090050048, WK2090000058), and the Students' Innovation and Entrepreneurship Foundation of USTC (CY2024G003B, CY2024G017A, CY2024C002A). We acknowledge the Experimental Center of Engineering and Material Sciences at USTC for the fabrication and measurement of samples. This work was partially carried out at the USTC Center for Micro and Nanoscale Research and Fabrication and Instruments Center for Physical Science, University of Science and Technology of China.

REFERENCES

(1) Ikushima, A. J.; Fujiwara, T.; Saito, K. Silica Glass: A Material for Photonics. *J. Appl. Phys.* **2000**, *88* (3), 1201−1213.

(2) Sugioka, K. *Microstructuring of Photosensitive Glass*; Springer: Berlin, Heidelberg, 2012.

(3) Rahaman, M. N.; Day, D. E.; Bal, B. S.; Fu, Q.; Jung, S. B.; Bonewald, L. F.; Tomsia, A. P. Bioactive Glass in Tissue Engineering. *Acta Biomater.* **2011**, *7* (6), 2355−2373.

(4) Hua, J. G.; Ren, H.; Huang, J. T.; Luan, M. L.; Chen, Q. D.; Juodkazis, S.; Sun, H. B. Laser-Induced Cavitation-Assisted True 3D

Nano-Sculpturing of Hard Materials. *Small* **2023**, *19* (24), No. 2207968.
(5) Suleski, T. J.; Te Kolste, R. D. Fabrication Trends for Free-Space Microoptics. *J. Lightwave Technol.* **2005**, *23* (2), 633−646.
(6) Collot, L.; Lefevreseguin, V.; Brune, M.; Raimond, J. M.; Haroche, S. Very High-Q Whispering-Gallery Mode Resonances Observed on Fused-Silica Microspheres. *Europhys. Lett.* **1993**, *23* (5), 327−334.
(7) Rossi, C.; Zhang, K.; Estève, D.; Alphonse, P.; Tailhades, P.; Vahlas, C. Nanoenergetic Materials for Mems: A Review. *J. Microelectromech. Syst.* **2007**, *16* (4), 919−931.
(8) Sugioka, K.; Cheng, Y.; Midorikawa, K. Three-Dimensional Micromachining of Glass Using Femtosecond Laser for Lab-on-a-Chip Device Manufacture. *Appl. Phys. A: Mater. Sci. Process.* **2005**, *81* (1), 1−10.
(9) Hu, Y. L.; Rao, S. L.; Wu, S. Z.; Wei, P. F.; Qiu, W. X.; Wu, D.; Xu, B.; Ni, J. C.; Yang, L.; Li, J. W.; Chu, J. R.; Sugioka, K. All-Glass 3D Optofluidic Microchip with Built-in Tunable Microlens Fabricated by Femtosecond Laser-Assisted Etching. *Adv. Opt. Mater.* **2018**, *6* (9), No. 1701299.
(10) Gissibl, T.; Thiele, S.; Herkommer, A.; Giessen, H. Sub-Micrometre Accurate Free-Form Optics by Three-Dimensional Printing on Single-Mode Fibres. *Nat. Commun.* **2016**, *7*, 11763.
(11) Hadibrata, W.; Wei, H. M.; Krishnaswamy, S.; Aydin, K. Inverse Design and 3D Printing of a Metalens on an Optical Fiber Tip for Direct Laser Lithography. *Nano Lett.* **2021**, *21* (6), 2422−2428.
(12) Ren, H. R.; Jang, J. Y.; Li, C. H.; Aigner, A.; Plidschun, M.; Kim, J.; Rho, J.; Schmidt, M. A.; Maier, S. A. An Achromatic Metafiber for Focusing and Imaging across the Entire Telecommunication Range. *Nat. Commun.* **2022**, *13* (1), 4183.
(13) Gissibl, T.; Thiele, S.; Herkommer, A.; Giessen, H. Two-Photon Direct Laser Writing of Ultracompact Multi-Lens Objectives. *Nat. Photonics* **2016**, *10* (8), 554−560.
(14) Thiele, S.; Arzenbacher, K.; Gissibl, T.; Giessen, H.; Herkommer, A. M. 3D-Printed Eagle Eye: Compound Microlens System for Foveated Imaging. *Sci. Adv.* **2017**, *3* (2), No. e1602655.
(15) Nguyen, D. T.; Meyers, C.; Yee, T. D.; Dudukovic, N. A.; Destino, J. F.; Zhu, C.; Duoss, E. B.; Baumann, T. F.; Suratwala, T.; Smay, J. E.; Dylla-Spears, R. 3D-Printed Transparent Glass. *Adv. Mater.* **2017**, *29* (26), No. 1701181.
(16) Kotz, F.; Arnold, K.; Bauer, W.; Schild, D.; Keller, N.; Sachsenheimer, K.; Nargang, T. M.; Richter, C.; Helmer, D.; Rapp, B. E. Three-Dimensional Printing of Transparent Fused Silica Glass. *Nature* **2017**, *544* (7650), 337−339.
(17) Liu, C.; Qian, B.; Liu, X. F.; Tong, L. M.; Qiu, J. R. Additive Manufacturing of Silica Glass Using Laser Stereolithography with a Top-Down Approach and Fast Debinding. *RSC Adv.* **2018**, *8* (29), 16344−16348.
(18) Li, Z. Y.; Jia, Y. W.; Duan, K.; Xiao, R.; Qiao, J. Y.; Liang, S. Y.; Wang, S. X.; Chen, J. Z.; Wu, H.; Lu, Y.; Wen, X. W. One-Photon Three-Dimensional Printed Fused Silica Glass with Sub-Micron Features. *Nat. Commun.* **2024**, *15* (1), 2689.
(19) Arita, R.; Iijima, M.; Fujishiro, Y.; Morita, S.; Furukawa, T.; Tatami, J.; Maruo, S. Rapid Three-Dimensional Structuring of Transparent Sio_2 Glass Using Interparticle Photo-Cross-Linkable Suspensions. *Commun. Mater.* **2020**, *1* (1), 30.
(20) Cai, P.; Guo, L.; Wang, H.; Li, J. M.; Li, J. T.; Qiu, Y. X.; Zhang, Q. M.; Lue, Q. T. Effects of Slurry Mixing Methods and Solid Loading on 3D Printed Silica Glass Parts Based on Dlp Stereolithography. *Ceram. Int.* **2020**, *46* (10), 16833−16841.
(21) Xu, H.; Cai, P.; Guo, J. X.; Guo, L.; Zhang, Q. M. Research on Additive Manufacturing Technology of High Solid Loading Silica Glass Slurry. *Mater. Lett.* **2024**, *373* (15), No. 137057.
(22) Toombs, J. T.; Luitz, M.; Cook, C. C.; Jenne, S.; Li, C. C.; Rapp, B. E.; Kotz-Helmer, F.; Taylor, H. K. Volumetric Additive Manufacturing of Silica Glass with Microscale Computed Axial Lithography. *Science* **2022**, *376* (6590), 308−312.
(23) Kotz, F.; Quick, A. S.; Risch, P.; Martin, T.; Hoose, T.; Thiel, M.; Helmer, D.; Rapp, B. E. Two-Photon Polymerization of Nanocomposites for the Fabrication of Transparent Fused Silica Glass Microstructures. *Adv. Mater.* **2021**, *33* (9), No. 2006341.
(24) Doualle, T.; Andre, J. C.; Gallais, L. 3D Printing of Silica Glass through a Multiphoton Polymerization Process. *Opt. Lett.* **2021**, *46* (2), 364−367.
(25) Wen, X. W.; Zhang, B. Y.; Wang, W. P.; Ye, F.; Yue, S.; Guo, H.; Gao, G. H.; Zhao, Y. S.; Fang, Q. Y.; Nguyen, C.; Zhang, X.; Bao, J. M.; Robinson, J. T.; Ajayan, P. M.; Lou, J. 3D-Printed Silica with Nanoscale Resolution. *Nat. Mater.* **2021**, *20* (11), 1506−1511.
(26) Prediger, R.; Kluck, S.; Hambitzer, L.; Sauter, D.; Kotz-Helmer, F. High-Resolution Structuring of Silica-Based Nanocomposites for the Fabrication of Transparent Multicomponent Glasses with Adjustable Properties. *Adv. Mater.* **2024**, *36* (44), No. 2407630.
(27) Moore, D. G.; Barbera, L.; Masania, K.; Studart, A. R. Three-Dimensional Printing of Multicomponent Glasses Using Phase-Separating Resins. *Nat. Mater.* **2020**, *19* (2), 212−217.
(28) Bauer, J.; Crook, C.; Baldacchini, T. A Sinterless, Low-Temperature Route to 3D Print Nanoscale Optical-Grade Glass. *Science* **2023**, *380* (6648), 960−966.
(29) Ye, P. R.; Hong, Z. H.; Loy, D. A.; Liang, R. G. Solvent-Free Silsesquioxane Self-Welding for 3D Printing Multi-Refractive Index Glass Objects. *Adv. Opt. Mater.* **2024**, *12* (23), No. 2400783.
(30) Zhu, D.; Jiang, S.; Liao, C.; Xu, L.; Wang, Y.; Liu, D.; Bao, W.; Wang, F.; Huang, H.; Weng, X.; Liu, L.; Qu, J.; Wang, Y. Ultrafast Laser 3D Nanolithography of Fiber-Integrated Silica Microdevices. *Nano Lett.* **2024**, *24* (31), 9734−9742.
(31) Hong, Z. H.; Ye, P. A. R.; Loy, D. A.; Liang, R. G. Three-Dimensional Printing of Glass Micro-Optics. *Optica* **2021**, *8* (6), 904−910.
(32) Hong, Z. H.; Ye, P. R.; Loy, D. A.; Liang, R. G. High-Precision Printing of Complex Glass Imaging Optics with Precondensed Liquid Silica Resin. *Adv. Sci.* **2022**, *9* (18), No. 2105595.
(33) Li, M.; Yue, L.; Rajan, A. C.; Yu, L.; Sahu, H.; Montgomery, S. M.; Ramprasad, R.; Qi, H. J. Low-Temperature 3D Printing of Transparent Silica Glass Microstructures. *Sci. Adv.* **2023**, *9* (40), No. eadi2958.
(34) Huang, P. H.; Laakso, M.; Edinger, P.; Hartwig, O.; Duesberg, G. S.; Lai, L. L.; Mayer, J.; Nyman, J.; Errando-Herranz, C.; Stemme, G.; Gylfason, K. B.; Niklaus, F. Three-Dimensional Printing of Silica Glass with Sub-Micrometer Resolution. *Nat. Commun.* **2023**, *14* (1), 3305.
(35) Lai, L. L.; Huang, P. H.; Stemme, G.; Niklaus, F.; Gylfason, K. B. 3D Printing of Glass Micro-Optics with Subwavelength Features on Optical Fiber Tips. *ACS Nano* **2024**, *18* (16), 10788−10797.
(36) Cooperstein, I.; Shukrun, E.; Press, O.; Kamyshny, A.; Magdassi, S. Additive Manufacturing of Transparent Silica Glass from Solutions. *ACS Appl. Mater. Interfaces* **2018**, *10* (22), 18879−18885.
(37) Li, B. N.; Li, Z. J.; Cooperstein, I.; Shan, W. Z.; Wang, S. P.; Jiang, B. X.; Zhang, L.; Magdassi, S.; He, J. Additive Manufacturing of Transparent Multi-Component Nanoporous Glasses. *Adv. Sci.* **2023**, *10* (35), No. 2305775.
(38) Lim, T. W.; Son, Y.; Yang, D. Y.; Pham, T. A.; Kim, D. P.; Yang, B. I.; Lee, K. S.; Park, S. H. Net Shape Manufacturing of Three-Dimensional Sicn Ceramic Microstructures Using an Isotropic Shrinkage Method by Introducing Shrinkage Guiders. *Int. J. Appl. Ceram. Technol.* **2008**, *5* (3), 258−264.
(39) Mori, T.; Wang, H.; Zhang, W.; Ser, C. C.; Arora, D.; Pan, C. F.; Li, H.; Niu, J. B.; Rahman, M. A.; Mori, T.; Koishi, H.; Yang, J. K. W. Pick and Place Process for Uniform Shrinking of 3D Printed Micro- and Nano-Architected Materials. *Nat. Commun.* **2023**, *14* (1), 5876.
(40) Liu, Y. J.; Wang, H.; Ho, J. F.; Ng, R. C.; Ng, R. J. H.; Hall-Chen, V. H.; Koay, E. H. H.; Dong, Z. G.; Liu, H. L.; Qiu, C. W.; Greer, J. R.; Yang, J. K. W. Structural Color Three-Dimensional Printing by Shrinking Photonic Crystals. *Nat. Commun.* **2019**, *10*, 4340.
(41) Herring, C. Effect of Change of Scale on Sintering Phenomena. *J. Appl. Phys.* **1950**, *21* (4), 301−303.

https://doi.org/10.1021/acsnano.5c09272
ACS Nano 2025, 19, 31643−31655

(42) Tang, D. N.; Wang, Y. S.; Li, Z.; Li, Y.; Hao, L. Coupling Additive Manufacturing and Low-Temperature Sintering: A Fast Processing Route of Silicate Glassy Matrix. *Rapid Prototyp. J.* **2022**, *28* (4), 676−685.
(43) Antonucci, J. M.; Dickens, S. H.; Fowler, B. O.; Xu, H. H. K.; McDonough, W. G. Chemistry of Silanes: Interfaces in Dental Polymers and Composites. *J. Res. Natl. Inst. Standards Technol.* **2005**, *110* (5), 541−558.
(44) Desponds, A.; Banyasz, A.; Chateau, D.; Tellal, A.; Venier, A.; Meille, S.; Montagnac, G.; Chevalier, J.; Andraud, C.; Baldeck, P. L.; Parola, S. 3D Printing and Pyrolysis of Optical Zro Nanostructures by Two-Photon Lithography: Reduced Shrinkage and Crystallization Mediated by Nanoparticles Seeds. *Small* **2021**, *17* (42), No. 2102486.
(45) Aubert, T.; Huang, J. Y.; Ma, K.; Hanrath, T.; Wiesner, U. Porous Cage-Derived Nanomaterial Inks for Direct and Internal Three-Dimensional Printing. *Nat. Commun.* **2020**, *11* (1), 4695.
(46) Huang, J. Y.; Xu, H.; Peratz, E.; Wu, D. Y.; Ober, C. K.; Hanrath, T. Three-Dimensional Printing of Hierarchical Porous Architectures. *Chem. Mater.* **2019**, *31* (24), 10017−10022.
(47) Ovsianikov, A.; Viertl, J.; Chichkov, B.; Oubaha, M.; MacCraith, B.; Sakellari, I.; Giakoumaki, A.; Gray, D.; Vamvakaki, M.; Farsari, M.; Fotakis, C. Ultra-Low Shrinkage Hybrid Photosensitive Material for Two-Photon Polymerization Microfabrication. *ACS Nano* **2008**, *2* (11), 2257−2262.
(48) Ramasinghe, R. L. P.; Liyanage, N. M. V. K. Synthesis of Nanosilica Using Acrylic Polymers as Surface Modifiers. In *2017 3rd International Moratuwa Engineering Research Conference (Mercon)*, Moratuwa, Sri Lanka, 2017.
(49) Schild, H. G. Thermal Degradation of Poly(Methacrylic Acid): Further Studies Applying Tga/Ftir. *J. Polym. Sci., Part A: Polym. Chem.* **1993**, *31* (9), 2403−2405.
(50) Zhou, Y. H.; Gu, Z. N. The Study of Removing Hydroxyl from Silica Glass. *J. Non-Cryst. Solids* **2006**, *352* (38−39), 4030−4033.
(51) Ikeda, H.; Fujino, S.; Kajiwara, T. Preparation of Sio_2-Pva Nanocomposite and Monolithic Transparent Silica Glass by Sintering. *J. Ceram. Soc. Jpn.* **2011**, *119* (1385), 65−69.
(52) Bertoluzza, A.; Fagnano, C.; Morelli, M. A.; Gottardi, V.; Guglielmi, M. Raman and Infrared Spectra on Silica Gel Evolving toward Glass. *J. Non-Cryst. Solids* **1982**, *48* (1), 117−128.
(53) Zhang, Q. L.; Hu, Y. W.; Feng, Y. W.; Sun, X. Y.; Duan, J. A. Critical Role of Water in Fused Silica Glass by Silica Nanopowder Sintering: Nanoparticle Dispersion. *J. Non-Cryst. Solids* **2023**, *609*, No. 122288.
(54) Guo, S. R.; Ali, M. A.; Mohamed, M. A.; Han, X. H.; Liu, X. F.; Qiu, J. R. Reduction of Injection Molded Silica Glass Defects and Enhancement of Glass Quality Water Debinding. *Mater. Chem. Front.* **2024**, *8* (5), 1400−1408.
(55) Bin Nun, M.; Gvishi, R.; Dana, Y.; Garcia, Y.; Marom, D. M.; Atar, N.; Porat, O.; Bar, G. Silica-Rich Sol-Gel Ink for Two-Photon Direct Laser Writing of Microscale Structures and Optical Elements. *Adv. Opt. Mater.* **2024**, *12* (27), No. 2400313.
(56) Geissberger, A. E.; Galeener, F. L. Raman Studies of Vitreous Sio_2 Versus Fictive Temperature. *Phys. Rev. B* **1983**, *28* (6), 3266−3271.
(57) Ikeda, H.; Fujino, S. Fabrication and Characterization of Porous Silica Monolith by Sintering Silica Nanoparticles. *J. Miner. Mater. Characterization Eng.* **2017**, *5* (03), 107−117.
(58) Bertoluzza, A.; Fagnano, C.; Morelli, M. A.; Guglielmi, M.; Scarinci, G.; Maliavski, N. Raman Spectra of Sio_2 Gel Glasses Prepared from Alkoxide, Colloidal and Amine Silicate Solutions. *J. Raman Spectrosc.* **1988**, *19* (4), 297−300.
(59) Bauer, J.; Izard, A. G.; Zhang, Y. F.; Baldacchini, T.; Valdevit, L. Programmable Mechanical Properties of Two-Photon Polymerized Materials: From Nanowires to Bulk. *Adv. Mater. Technol.* **2019**, *4* (9), No. 1900146.
(60) Li, Z. Y.; Jia, Y. W.; Xiao, R.; Chen, J. Z.; Wu, H.; Wen, X. W.; Lu, Y. 3D-Printed Fused Silica Glass Microlattice as Mechanical Metamaterial. *Cell Rep. Phys. Sci.* **2024**, *5* (9), No. 102172.
(61) Du, Y.; He, H. B.; Jin, Y. X.; Kong, F. Y.; Guan, H. Y.; Fan, Z. X. Graded Porous Glasses for Antireflective Applications Formed by Chemical Treatment. *Appl. Surf. Sci.* **2012**, *258* (17), 6431−6435.
(62) Yoldas, B. E.; Partlow, D. P. Wide Spectrum Antireflective Coating for Fused-Silica and Other Glasses. *Appl. Opt.* **1984**, *23* (9), 1418−1424.
(63) Huang, Y.; Qin, Y. L.; Tu, P.; Zhang, Q.; Zhao, M.; Yang, Z. Y. High Fill Factor Microlens Array Fabrication Using Direct Laser Writing and Its Application in Wavefront Detection. *Opt. Lett.* **2020**, *45* (16), 4460−4463.
(64) Zhang, H.; Li, F.; Song, H. Y.; Liu, Y. Q.; Huang, L.; Zhao, S. Q.; Xiong, Z.; Wang, Z. X.; Dong, Y. J.; Liu, H. Random Silica-Glass Microlens Arrays Based on the Molding Technology of Photocurable Nanocomposites. *ACS Appl. Mater. Interfaces* **2023**, *15* (19), 19230−19240.
(65) Wang, H.; Pan, C. F.; Li, C.; Menghrajani, K. S.; Schmidt, M. A.; Li, A. L.; Fan, F.; Zhou, Y.; Zhang, W.; Wang, H. T.; Nair, P. N. S.; Chan, J. Y. E.; Mori, T.; Hu, Y. Q.; Hu, G. W.; Maier, S. A.; Ren, H. R.; Duan, H. G.; Yang, J. K. W. Two-Photon Polymerization Lithography for Imaging Optics. *Int. J. Extrem. Manuf.* **2024**, *6* (4), No. 042002.
(66) Ottevaere, H.; Cox, R.; Herzig, H. P.; Miyashita, T.; Naessens, K.; Taghizadeh, M.; Völkel, R.; Woo, H. J.; Thienpont, H. Comparing Glass and Plastic Refractive Microlenses Fabricated with Different Technologies. *Journal of Optics a-Pure and Applied Optics* **2006**, *8* (7), S407−S429.
(67) Ruchka, P.; Kushwaha, A.; Marathe, J. A.; Xiang, L.; Chen, R. Y.; Kirk, R.; Tan, J. T. M.; Bursill, C. A.; Verjans, J.; Thiele, S.; Fitridge, R.; Mclaughlin, R. A.; Psaltis, P. J.; Giessen, H.; Li, J. W. 3D-Printed Micro-Axicon Enables Extended Depth-of-Focus Intravascular Optical Coherence Tomography. *Advanced Photonics* **2025**, *7* (2), No. 026003.
(68) Li, J. W.; Thiele, S.; Quirk, B. C.; Kirk, R. W.; Verjans, J. W.; Akers, E.; Bursill, C. A.; Nicholls, S. J.; Herkommer, A. M.; Giessen, H.; McLaughlin, R. A. Ultrathin Monolithic 3D Printed Optical Coherence Tomography Endoscopy for Preclinical and Clinical Use. *Light: Sci. Appl.* **2020**, *9*, 124.
(69) Chen, J. C.; Li, J.; Li, B. N.; Chen, Z. C.; Bai, X.; Zhang, L.; He, J. Thermal Reduction-Triggered Full-Color Tuning of Eu^{3+}/Eu^{2+}/Tb^{3+} Co-Doped Sintered Nanoporous Al_2o_3-Sio_2 Glass for Wleds. *J. Non-Cryst. Solids* **2023**, *613* (1), No. 122329.
(70) Limongi, T.; Susa, F.; Allione, M.; di Fabrizio, E. Drug Delivery Applications of Three-Dimensional Printed (3dp) Mesoporous Scaffolds. *Pharmaceutics* **2020**, *12* (9), 851.

https://doi.org/10.1021/acsnano.5c09272
ACS Nano 2025, 19, 31643−31655